

INVESTIGATION OF HEAT-AFFECTED 304L SS POWDER AND ITS EFFECT ON BUILT PARTS IN SELECTIVE LASER MELTING

Caitlin S. Kriewall¹, Austin T. Sutton², Ming C. Leu², Joseph W. Newkirk¹, Ben Brown^{2,3}

¹Department of Materials Science and Engineering, Missouri University of Science and
Technology, Rolla, MO 65409

²Department of Mechanical and Aerospace Engineering, Missouri University of Science and
Technology, Rolla, MO 65409

³Department of Energy's Kansas City National Security Campus Managed by
Honeywell FM&T, Kansas City, MO 64147

Abstract

Selective laser melting (SLM) is a powder bed based additive manufacturing process in which a layer of powder is laid over the surface of a substrate and a laser with sufficient energy is employed to selectively melt particles to build a part layer by layer. During the SLM process, dark smoke was observed coming off of the powder bed surface where the laser was interacting with powder. This phenomenon resulted from heat-affected powder that was visibly different than the base powder. Since the concentration of the heat-affected powder differs throughout the build chamber as a result of the recirculating argon gas flow, powder samples from different regions were collected for analysis. The heat-affected powder samples were analyzed by scanning electron microscopy (SEM), x-ray photoelectron spectroscopy (XPS), and x-ray diffraction (XRD) in order to distinguish differences between the heat-affected powder and the base 304L stainless steel powder. The influences of the heat-affected powder on the microstructure and tensile properties of parts built in different areas of the build chamber are also investigated.

Introduction

Additive Manufacturing (AM) is a class of layer-based techniques used primarily for the creation of parts with complex geometry that are otherwise impossible or impractical to create through conventional means [1]. This technology enables the direct translation of Computer-Aided Design (CAD) data into tangible parts thereby decreasing the amount of design limitations imposed by manufacturability constraints [2]. As the AM industry reaches a stage of maturity since its conception with stereolithography in 1987 [3], the goal of being able to produce functional components becomes a priority. Although there exist many process variants that each can be categorized by the state of the starting material [4], a search of the existing literature indicates that many of the successful attempts to produce functional AM components stem from using powder as the raw input material [5].

Among the available powder-based additive methods is the selective laser melting (SLM) process in which successive layers of powder are selectively bonded by a laser. Rather than sinter particles together by forming bridges or through the use of a binder as in selective laser sintering (SLS), the consolidation mechanism in SLM relies on the melting of material to form dense parts in a single step with little to no post-processing. However, as with any new

manufacturing process there exists a research and development phase aimed at exploiting the true potential of this technology in order to solve crucial issues influencing part quality. A significant amount of research in SLM is focused on the optimization of process parameters for specific materials to produce parts of acceptable quality [6–9]. Often, variables such as laser power, scanning speed, hatch spacing, and layer thickness are tuned until satisfaction with part properties is met. Other work is directed towards understanding the relationship between input material properties and part characteristics [5,10–17]. These studies observe not only the influences of morphological characteristics of powder particles on the parts that are built but also the ramifications of differing chemistry and powder reuse.

In order to understand the fundamentals of the SLM process, researchers have also focused on rigorous modeling of the melting process [18–21]. In these simulations, the interaction between the laser and the powder bed can be observed. It has been noticed that the melt pool is a complex environment with fluid flow driven by Marangoni convection as a consequence of steep thermal gradients. It is also evident that a certain amount of vaporization of volatile elements and potentially small particles takes place due to a high energy input. This vaporization leads to two types of heat-affected powder: laser spatter and condensate. Laser spatter is a direct result of the upsurge of vaporized gases through the melt pool causing molten material to be ejected as a result of melt pool instabilities [22–24]. Once ejected, solidification of the molten material occurs while in the chamber atmosphere where it is later redeposited elsewhere in the powder bed. These particles have been proven to be chemically different from the base powder [22], and could potentially alter the properties of the parts in which it is redeposited during the build process. The other form of heat-affected powder, condensate, forms as a result of the vaporized material above the melt pool rapidly condensing [25,26]. As such, the majority of these particles are small and responsible for sticking to the surfaces within the build chamber. However, due to their small size agglomeration can occur leading to the formation of larger particles [25] heavy enough to settle inside the powder bed. If not properly removed, condensate can also interact with the laser beam causing attenuation and scattering [23–27], both of which can have negative impacts on the part quality.

In order to mitigate the interference between the laser and condensate cloud, the recirculating gas flow across the build area is optimized to be as uniform and high as possible without disturbing the arrangement of powder particles in each layer. Ferrar et al. [26] modeled the build chamber as well as the inlet and outlet gas flow configurations for the SLM machine under consideration so that a CFD simulation could be run to visualize the flow across the powder bed. It was found that the flow field was inconsistent producing regions of high gas flow and relatively stagnant flow in others. The inlet manifold was then optimized to improve the uniformity of flow across the bed. Another study [25] observed the influence of a varying gas flow on the surface irregularities of built parts in addition to the formation of material defects in regards to pores. The results showed that a reduced gas flow rate caused more interaction between the laser and the condensate cloud thereby increasing porosity, top surface roughness, and the overall width of the laser scan. However, material properties were not quantified so as to observe the degree of influence of the reduced gas recirculation speed. Moreover, a thorough search of the literature suggests that the influences of condensate on part properties in the SLM process is sparse thereby warranting an investigation to be completed.

Therefore, this study attempts to shed light regarding the influence of heat-affected powder on the tensile properties of as-built components. It was realized that condensate may not only interfere with the laser beam, but may also be redeposited onto other parts in the build area. To observe the effect of both, the pump speed was varied and a region upstream of the tensile specimens was selectively melted for heat-affected powder production (Figure 1). In addition to the tensile properties, part porosity was measured to observe potential correlations between pore formation and degradation in strength. Since very little research characterizes heat-affected powder, samples were collected and analyzed in terms of particle size distribution and shape by using an ASPEX SEM, surface chemistry with the aid of x-ray photoelectron spectroscopy (XPS), and x-ray diffraction (XRD) for insight into crystal structure. These results were then compared to the base powder in addition to powder samples collected around the parts built in various locations.

Experimental

The starting powder used was a gas atomized 304L stainless steel powder purchased from LPW. The chemical composition of the powder was provided by LPW and is given in Table 1. Prior to being placed in the SLM machine, the powder was passed through a 63 μm mesh sieve that had been purged with argon gas. Once sieved, the powder was processed using a Renishaw AM250 SLM machine which contained a pulsed Nd-YAG laser with a Gaussian profile beam intensity and a wavelength of 1070 nm. After calibrating the focal offset of the laser, the diameter of the beam spot on the powder bed was approximately 70 μm .

Table 1: Chemical composition of the base 304L stainless steel powder

Element	C	Cr	Cu	Fe	Mn	N	Ni	O	P	S	Si
Wt %	0.015	18.5	< 0.1	69.3	1.4	0.09	9.9	0.02	0.012	0.004	0.63

Four builds were completed in order to study the effect of the heat-affected powder on the built parts. In each of the builds, a stack of Automated Ball Indenter (ABI) tensile specimens 20 mm tall were built at 5 different locations across the diagonal of the build chamber. ABI tensile specimens have a 1" (25.4 mm) total length with a 0.3" (7.6 mm) reduced gauge section and a thickness of 0.06" (1.5 mm). Build 1 incorporated a nominal pump speed ($\approx 400 \text{ ft}^3/\text{min}$)

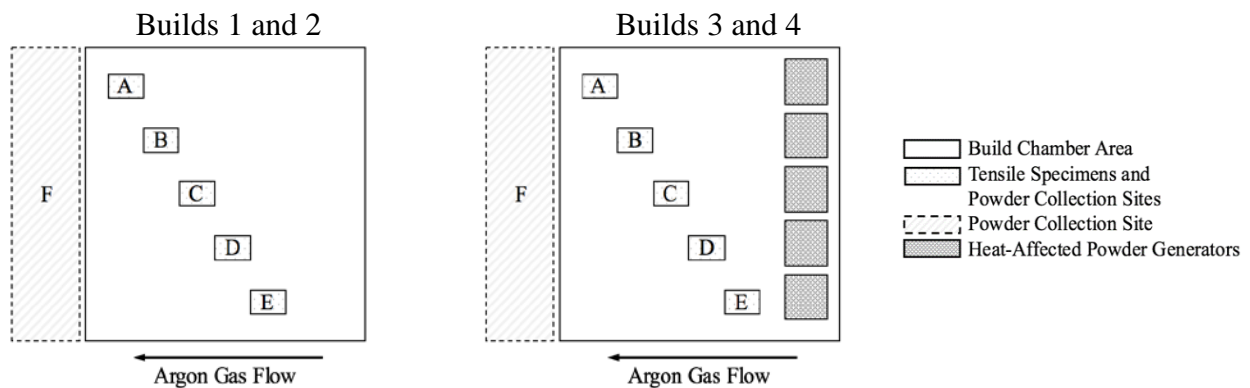


Figure 1: Experimental setup of the four builds, where Builds 1 and 3 had nominal argon gas pump speed and Builds 2 and 4 had reduced argon gas pump speed

while Build 2 had a lower pump speed ($\approx 210 \text{ ft}^3/\text{min}$). Builds 3 and 4 incorporated extra square parts to the right of the build chamber to act as heat-affected power generators. As before, Build 3 had a higher pump speed and Build 4 had a lower pump speed. The geometry of these builds is shown in Figure 1. After the build was completed, powder samples at each location were collected as well as samples of powder to the left of the build area, in Location F, where visibly different powder had been noticed in previous experiments. A band saw was used to remove the tensile specimen stacks from the build plate and an EDM was used to slice five tensile specimens at each location (a total of 100 tensile specimens) that were approximately 1.5 mm thick.

Morphological characterization was performed using an ASPEX 1020 SEM equipped with automated feature analysis (AFA) to determine the projected area and perimeter of each particle in a given powder sample for a sample of sieved 304L SS and a sample taken from Location F. Additional characterization was performed on the sieved 304L SS sample as well as the powder samples taken from Location A - F using a Panalytical X'pert Pro Multi-Purpose Diffractometer for insight into the particle microstructure. The surface of the powder particles was studied with a Kratos Axis 165 Photoelectron Spectrometer XPS instrument where the sample was sputtered for 1 minute prior to spectral acquisition. For the XPS analysis, the x-ray spot size used was $700 \times 300 \mu\text{m}$ to ensure that the results were representative of the powder sample.

Characterization of the as-built parts included tensile tests performed using an Automated Ball Indenter (ABI) Universal Testing Machine with a constant strain rate of $4.77 \times 10^{-4} \text{ s}^{-1}$. Tensile specimens were ground with 320 and 600 grit abrasive paper prior to testing. Density measurements were taken in accordance with ASTM B311 as well as surface roughness measurements using a Hirox KH-8700 Digital Microscope. Specimens were polished and electrolytically etched for 6 seconds using a 60:40 volume percent of nitric acid to water and 1 V. Optical micrographs were then obtained using a Nikon Epiphot 200 Microscope to compare the resulting microstructure.

Results and Discussion

Powder Characterization

Powder samples were first analyzed using the ASPEX 1020 SEM. Figure 2 shows a comparison of the base 304L SS powder and powder that was found in Location F of the build chamber. Overall, the heat-affected powder was morphologically similar in that it was still spherical. However, some anomalous particles were observed that appeared to have dark spots covering the surface. A standardless energy dispersive x-ray spectroscopy (EDS) scan was performed on the particles with dark spots which indicated a higher amount of silicon and manganese content compared to the base powder.

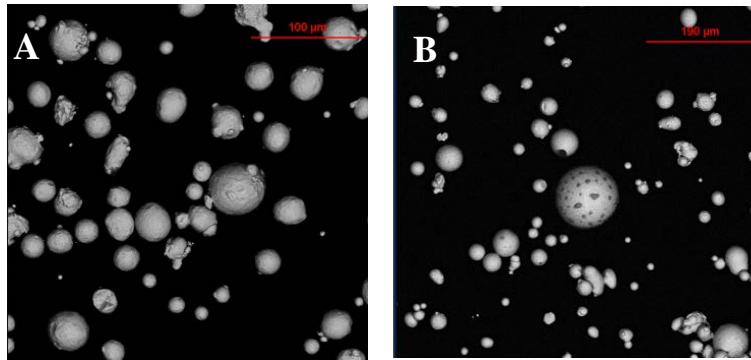


Figure 2: SEM micrographs of (A) sieved 304L stainless steel powder and (B) the heat-affected powder collected from Location F.

The appearance of dark regions on the surface of heat-affected powder particles with the knowledge that silicon and manganese have a high affinity for oxygen suggests that these are oxide islands. A similar phenomenon was reported by Simonelli et al. [22] for 316L stainless steel in studying the formation of laser spatter. Although condensate is inherently different from laser spatter in that it forms from a metallic vapor cloud instead of solidifying from a molten state in the build chamber atmosphere, it appears that the formation of these oxide islands is related primarily to the extremely high temperatures encountered by these particulates. Even with the small solidification times experienced, it is possible that the temperature is large enough to cause a significant amount of silicon and manganese diffusion to the outer surfaces of the particles. However, the thickness of the oxides is still unknown and will require further investigation.

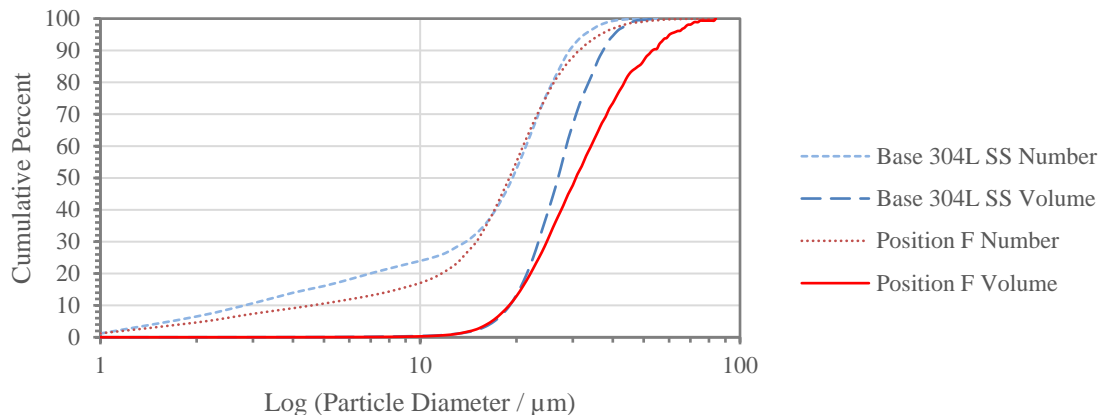


Figure 3: Cumulative number and frequency particle size distributions for the base 304L SS powder and the heat-affected powder found in Location F

Particle size distributions (both number distribution and volume distribution) obtained using the ASPEX SEM's AFA are shown in Figure 3. For each sample, over 6000 powder particles were analyzed to obtain the distribution. The heat-affected powder contained particles that were larger than any found in the base 304L SS powder, where the largest particle (84 µm)

was 30 μm larger than the largest particle found in the base 304L SS powder. At this point, it is important to note that the sampling of the heat-affected powder was done close to the gas flow exit. In this location it is likely that the larger heat-affected powder particles were only collected as they were not small enough to pass through the filter. Although this skews the measured particle size distribution, it is noteworthy that the large heat-affected powder particles were most likely dispersed throughout the powder bed while the smaller particles remained in the chamber atmosphere. The presence of large particles could indicate that this heat-affected powder contains spatter, however it could also be due to agglomeration of the fines as well. Circularity values were also found for each of the powder samples and the values for the base 304L SS powder and the powder obtained from Location F were 0.88 and 0.84, respectively.

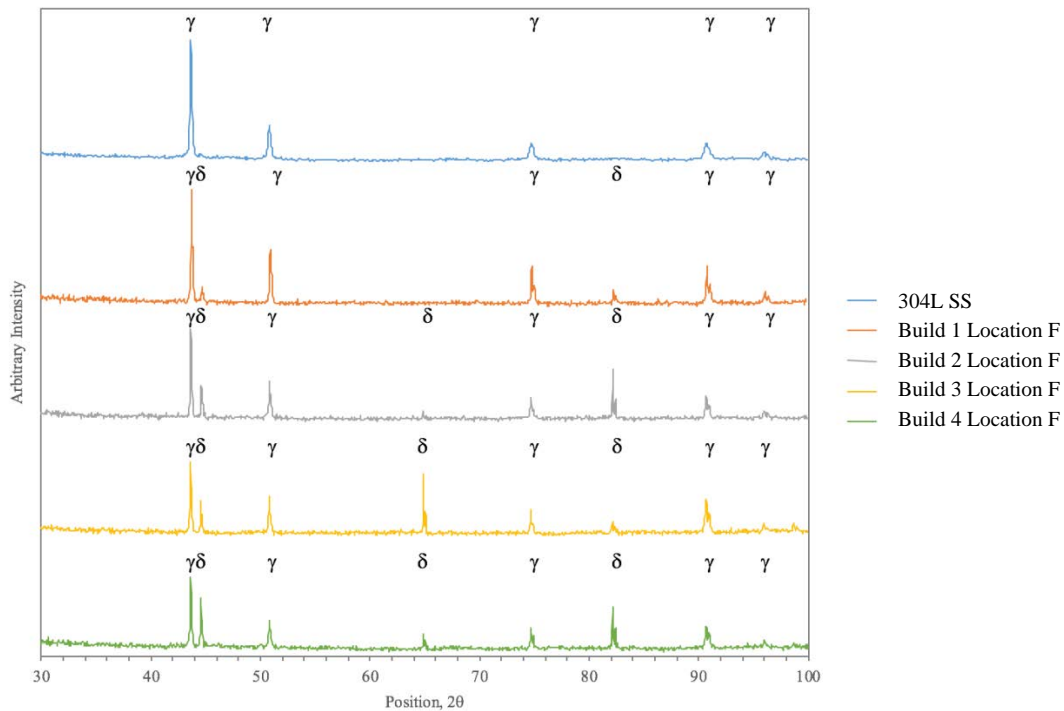


Figure 4: XRD spectra of the base 304L SS powder and the powder collected from Location F from each of the four builds.

Figure 4 shows the XRD spectra of the base 304L stainless steel powder compared to the powder collected from Location F from each of the 4 builds. The XRD spectra revealed that while the base 304L SS powder was completely γ -austenite, the heat-affected powders from Location F all had varying degrees of δ -ferrite in their microstructure. This result showed that this powder had been heated to the point of melting, and upon solidification the transformation from δ -ferrite to γ -austenite was kinetically inhibited due to the high cooling rate [28]. The spectra show that there are different amounts of the δ -ferrite in the samples, indicating varying amounts of heat-affected powder. Compared to Build 2, Build 1 had a higher argon flow rate. This enabled more of the heat-affected powder to exit the build chamber through the hole on the left wall, whereas it was simply collected in Build 2. Builds 3 and 4 follow the same logic, however the concentration of δ -ferrite in these samples is higher due to the extra parts built that generated more heat-affected powder. XRD spectra were also collected on various powder

samples from Locations A-E of several builds, however only peaks corresponding to γ -austenite were found. Therefore, if there was δ -ferrite (and therefore heat-affected powder) in the powder samples taken from inside the build chamber, it was not detectable by XRD.

XPS samples were taken from a small number of powder samples due to the time and cost of the instrument. The samples consisted of base 304L SS powder, powder from Location F, 2E, 3E, 4A, and 4E. The results from the survey spectra of the XPS analysis are summarized in Table 2. First, these results show how different the surface layers of the powder particles were to the bulk chemistry (shown in Table 1). The high content of carbon was likely due to contamination from carbon that had condensed on the sample from the air. The other concentrations indicated that the detected photoelectrons were ejected from the oxide layer. Powder samples taken from inside the build chamber showed chemistry that was more consistent with the base 304L SS powder, although decreases in Mn were observed in Build 4 Locations A and E. When comparing the data from different locations, the main element that was changed was Si, where the concentration was increased in the heat-affected powder. The extra Si could only come from two places, namely, inside the powder particle or outside the powder particle. Although the initial concentration of Si was only 0.63 wt %, it is possible due to the high temperatures experienced by the powder that diffusion through the bulk occurred, as has been noted as a possibility due to the high volatility of Si [22]. Furthermore, the wiper in the Renishaw AM250 is made of silicone, which could provide a possible source for the extra Si. A bulk chemistry validation will be required in the future to determine the source of the extra Si. High resolution spectra were taken for Cr, Mn, Si, and Fe, however these did not reveal any significant differences between the oxidation states of the elements in the powder particles.

Table 2: Results from the survey spectra of the XPS analysis on various powder samples.

Element	304L SS	Location F	2E	3E	4A	4E
C	5	6	5	4	8	5
O	28	33	28	31	32	32
N	-	-	-	-	1	-
Ni	-	-	-	3	-	-
Si	5	19	5	6	5	5
Cr	6	6	8	10	10	13
Mn	20	17	20	17	9	11
Fe	37	18	36	37	35	33

Part Characterization

Samples from all locations of the four builds were polished and etched and, in order for a comparison, the optical micrographs from Location E are shown in Figure 5. The build direction is normal to the plane of the paper, so the micrographs show the hatch spacing. What can be easily seen from these micrographs was that Builds 1 and 3, with the higher argon gas flow rate, had less porosity than Builds 2 and 4, although porosity was found in all of the specimens. Very

large pores were prevalent in Location D and E of Builds 2 and 4, where the degree of porosity was worse for Build 4 where the extra parts were built to generate more heat-affected powder.

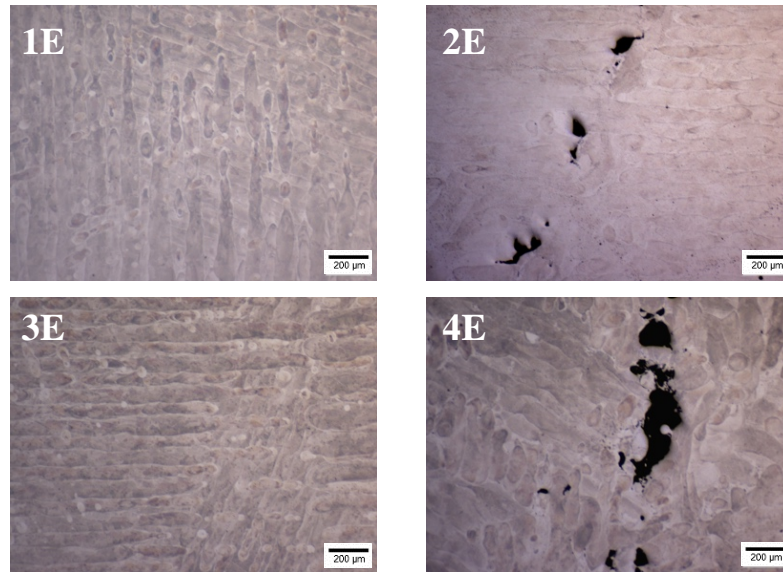


Figure 3: Optical micrographs of samples taken from Location E of each of the four builds. The print direction for these builds is normal to the plane of the paper.

The results from the tensile tests are shown in Table 3. For each build and location, the values shown are the average of 5 different tensile tests. For all locations in Build 1, both yield strength and UTS values were consistent within a 95% confidence interval. However, in Builds 2 and 4, Locations D and E showed a statistically significant decrease in properties. Consider Location E, where corresponding micrographs are shown in Figure 5. When looking at yield strength, for example, 2E and 4E both showed a decrease compared to 1E and 3E. Comparing this to the optical micrographs and the porosity that is present, it is obvious that the porosity had a detrimental effect on the part properties. Considering Build 4, the extra parts paired with the lower argon flow rate could have led to lowered part properties by redepositing some heat-affected powder onto other nearby parts. However, the decrease in properties for Build 2 is harder to explain. If it was just redeposition of heat-affected powder due to the slow argon flow rate, it would be expected that this would be found in all locations, because none of the parts are down stream of other parts. It would also be expected to see a decrease in properties at the left of the build chamber (Locations A and B) because large amounts of heat-affected powder are found in Location F, however this was not observed. Theories for the location of the decrease in properties are offered at the end of this section. A final observation for the tensile results was that Build 4 showed a significant decrease in UTS in all locations compared to those locations in Builds 1 – 3.

Table 3: Tensile testing results from five tensile specimens at each location of the four builds

	Elongation (%)	Area Reduction (%)	Yield Strength (MPa)	UTS (MPa)
1A	51.8 ± 0.99	58.4 ± 2.86	486 ± 2.72	666 ± 1.67
1B	55.3 ± 3.82	59.3 ± 3.13	484 ± 3.58	669 ± 3.83
1C	54.5 ± 3.14	58.3 ± 1.27	477 ± 1.97	662 ± 2.73
1D	53.7 ± 1.40	57.2 ± 3.05	474 ± 1.04	654 ± 4.83
1E	53.0 ± 0.97	57.5 ± 1.40	480 ± 2.98	668 ± 2.45
2A	54.4 ± 2.73	60.8 ± 2.54	477 ± 2.78	666 ± 1.78
2B	55.9 ± 2.95	59.7 ± 1.85	477 ± 4.80	659 ± 5.19
2C	54.2 ± 3.18	57.8 ± 1.28	481 ± 1.41	666 ± 2.69
2D	53.4 ± 2.64	58.6 ± 1.11	467 ± 4.24	656 ± 6.52
2E	46.8 ± 2.07	57.8 ± 2.54	447 ± 1.63	623 ± 1.90
3A	57.1 ± 1.81	60.2 ± 1.45	485 ± 4.19	664 ± 2.75
3B	55.7 ± 2.89	61.3 ± 2.26	483 ± 6.04	668 ± 5.23
3C	56.5 ± 2.06	57.7 ± 1.50	491 ± 2.52	676 ± 2.28
3D	55.1 ± 3.31	58.2 ± 0.96	472 ± 5.04	650 ± 3.69
3E	54.7 ± 0.88	58.2 ± 2.64	479 ± 4.88	654 ± 6.69
4A	53.4 ± 1.41	62.4 ± 1.79	470 ± 4.40	645 ± 5.53
4B	53.1 ± 1.87	59.7 ± 1.39	474 ± 4.09	646 ± 4.36
4C	53.3 ± 2.87	59.2 ± 0.65	464 ± 4.81	635 ± 7.38
4D	52.1 ± 2.47	53.9 ± 2.24	451 ± 3.22	629 ± 4.01
4E	41.5 ± 3.89	47.2 ± 5.18	427 ± 2.16	596 ± 6.00

The results of the density measurements compared with yield strength and UTS are shown in Figure 6, where they are grouped by location in the build chamber and patterns were used for the relative density to ease in the interpretation of the results. The relative density was calculated compared to the skeletal density of the 304L stainless steel SLM material (7.95 g/cc). The density measurements indicated that Location E showed the lowest densities compared to the other locations of the same build when considering Builds 2, 3, and 4, where the decrease was more drastic for Builds 3 and 4. This reveals that the location compared to other parts is an important factor. Additionally, Build 4 showed the lowest densities at every location, indicating that the gas flow rate is also a critical factor when multiple parts are being built. The density measurements correlate well with the yield strength and UTS values, where a lower density results in a decrease of strength for all cases.

Finally, surface roughness measurements were taken on the four builds at each location on surfaces perpendicular to the build direction. The results from this analysis are shown in Figure 7, where the value R_z represents the difference between the bottom and the top most surface. There was some variation across the locations of the builds; however, the obvious difference lies in Build 4, where higher surface roughness values were recorded for every location. This shows that when parts were at the same location with respect to the argon gas

flow, there were effects on the final part surface finish. Build 4 Location E had the highest surface roughness values likely due to it being the closest to the extra parts that were built.

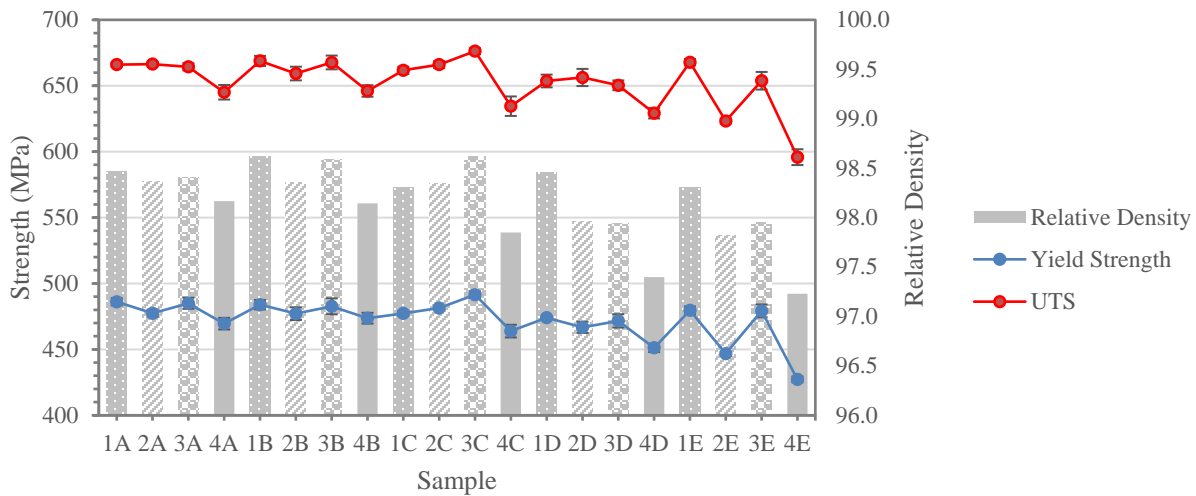


Figure 4: Comparison of the ultimate tensile strength, yield strength, and relative density

Based on the results, it can be noted that the gas flow rate as well as the location of the parts relative to other parts are important aspects in the SLM process. When parts are downstream of other parts, the heat-affected powder can redeposit on nearby locations thereby increasing local layer thicknesses [25]. This decreases the energy density thereby resulting in an increase in part porosity that is ultimately detrimental to the final part properties. However, this study yielded an unexpected result in that large amounts of heat-affected powder were collected to the left of the build chamber (Location F), so it was thought that the left side of the chamber would have more adverse effects due to the heat-affected powder. However, it was found that Locations D and E saw the most significant decrease in properties. Therefore, there has to be some other phenomenon occurring during the process. One possibility is that there could be turbulent flow in the build chamber. The Renishaw AM 250 allows gas to flow through 6 valves, not just at one specific location. So the gas could be interacting with gas from other nozzles causing some undesirable effects, such as dead zones or areas of high flow. Another possibility is that during the build process, the formation of condensate powder clouds de-focus the laser in addition to beam attenuation. At different locations, the laser beam has different interactions with the condensate cloud. If this is the case, the right side of the build chamber has some aspect that induces the interaction of the condensate cloud and the laser. More studies are necessary to determine the cause of why Locations D and E were the most effected.

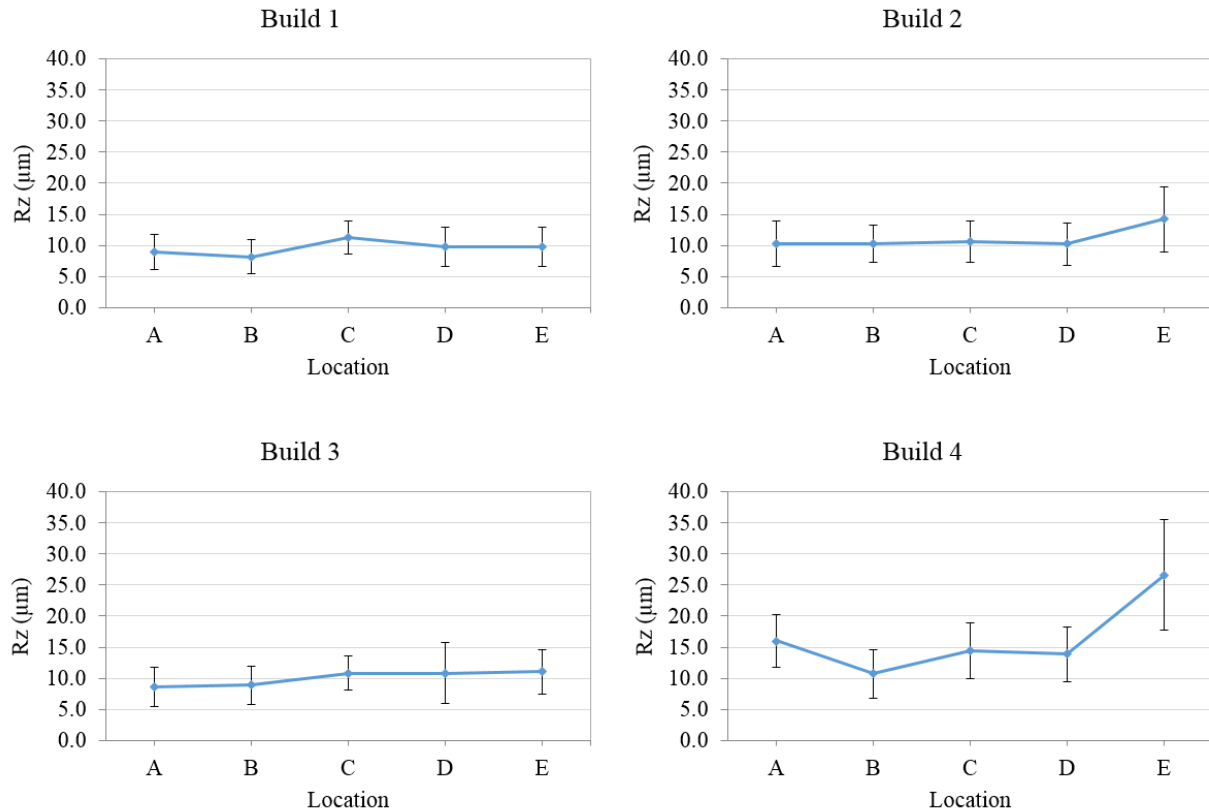


Figure 5: Rz surface roughness measurement for the four builds at each location

Conclusions and Future Work

The powder characterization study described in this paper showed that the powder collected to the left of the build chamber (Location F) did contain some large particles as a consequence of particle agglomeration and/or laser spatter. In addition to the fines being deposited on the chamber walls and being captured in the gas flow filter, this ultimately skews the particle size distribution towards being coarser than the base powder. As such, there is likely a deposition of large particles that occurs in each layer during the build process potentially shifting the average particle size of the powder with continued reuse. The average circularity values showed a 5% difference between the base powder and the heat-affected powder, where there was a decrease from 0.88 to 0.84, respectively. XRD values indicated that powder collected from Location F had been heated to the point of melting, where the fast cooling rate resulted in retained δ -ferrite in the microstructure. XRD was unable to detect any δ -ferrite on powder samples taken from inside the build chamber (Locations A-E). XPS analysis of the heat-affected showed elevated amounts of Si in the surface layers of powder particles. However, samples taken from inside the build chamber yielded results similar to the base 304L SS powder. In the future, a bulk chemistry analysis using ICPS will be performed to enable other insights to the changes that the powder underwent. These results should give insight to the elevated Si levels as to whether they were due to diffusion from the bulk of the particle or from outside the particle. The powder characterization results also indicated that characterization methods able to detect small

concentrations of heat-affected powder need to be determined, as the current powder characterization methods would have predicted no difference in final part properties where that was not what was observed.

Part characterization revealed that porosity was found in all of the built parts, where large pores could be found in builds and locations such as 2E, 4D, and 4E. Tensile tests were able to detect differences within a 95% confidence interval in Location E for Builds 2 and 4 compared to the other locations of the same build. Tensile tests also revealed that Build 1 showed consistency while Build 4 showed a decrease in UTS for all locations compared to the same locations for Builds 1-3. Density measurements were in agreement with the tensile results, where the common phenomena of lower density corresponded well to a decrease in strength. Finally, the surface roughness showed that Build 4 had a rougher surface finish on sides perpendicular to the build direction. Bulk chemistry verifications of the built parts will be completed in the future to see if the chemistry was different due to redeposited powder.

Although the results were consistent with each other, they were not expected. It was initially thought that the left side of the build chamber would see the most redeposited heat-affected powder as large amounts of heat-affected powder are found to the left of the build chamber, in Location F. However, Locations D and E showed a larger decrease in properties. This shows that it was not simply the gas flow controlling how the heat-affected powder was redeposited. Further studies into why Locations D and E are inferior to other locations must be performed to pinpoint the reason for this observation.

Acknowledgments

This work has been funded by Honeywell Federal Manufacturing & Technologies under Contract No. DE-NA0002839 with the U.S. Department of Energy. The United States Government retains and the publisher, by accepting the article for publication, acknowledges that the United States Government retains a nonexclusive, paid up, irrevocable, world-wide license to publish or reproduce the published form of this manuscript, or allow others to do so, for the United States Government purposes.

References

- [1] N. Guo, M.C. Leu, Additive manufacturing: Technology, applications and research needs, *Front. Mech. Eng.* 8 (2013) 215–243. doi:10.1007/s11465-013-0248-8.
- [2] E.C. Santos, M. Shiomi, K. Osakada, T. Laoui, Rapid manufacturing of metal components by laser forming, *Int. J. Mach. Tools Manuf.* 46 (2006) 1459–1468. doi:10.1016/j.ijmachtools.2005.09.005.
- [3] C.W. Hull, Apparatus for production of threedimensional objects by stereolithography, U.S. patent no. 4575330, 1986.
- [4] J.P. Kruth, Material Incess Manufacturing by Rapid Prototyping Techniques, *CIRP Ann. - Manuf. Technol.* 40 (1991) 603–614. doi:10.1016/S0007-8506(07)61136-6.

- [5] A. Simchi, The role of particle size on the laser sintering of iron powder, *Metall. Mater. Trans. B.* 35 (2004) 937–948. doi:10.1007/s11663-004-0088-3.
- [6] L. Thijs, F. Verhaeghe, T. Craeghs, J. Van Humbeeck, J.P. Kruth, A study of the microstructural evolution during selective laser melting of Ti-6Al-4V, *Acta Mater.* 58 (2010) 3303–3312. doi:10.1016/j.actamat.2010.02.004.
- [7] M. Averyanova, E. Cicala, P. Bertrand, D. Grevey, Experimental design approach to optimize selective laser melting of martensitic 17-4 PH powder: part I – single laser tracks and first layer, *Rapid Prototyp. J.* 18 (2012) 28–37. doi:10.1108/13552541211193476.
- [8] L.E. Murr, E. Martinez, J. Hernandez, S. Collins, K.N. Amato, S.M. Gaytan, P.W. Shindo, Microstructures and properties of 17-4 PH stainless steel fabricated by selective laser melting, *J. Mater. Res. Technol.* 1 (2012) 167–177. doi:10.1016/S2238-7854(12)70029-7.
- [9] X. Zhao, J. Chen, X. Lin, W. Huang, Study on microstructure and mechanical properties of laser rapid forming Inconel 718, *Mater. Sci. Eng. A.* 478 (2008) 119–124. doi:10.1016/j.msea.2007.05.079.
- [10] K. Abd-Elghany, D.L. Bourell, Property evaluation of 304L stainless steel fabricated by selective laser melting, *Rapid Prototyp. J.* 18 (2012) 420–428. doi:10.1108/13552541211250418.
- [11] E.O. Olakanmi, Selective laser sintering/melting (SLS/SLM) of pure Al, Al-Mg, and Al-Si powders: Effect of processing conditions and powder properties, *J. Mater. Process. Technol.* 213 (2013) 1387–1405. doi:10.1016/j.jmatprotec.2013.03.009.
- [12] B. Liu, R. Wildman, C. Tuck, I. Ashcroft, R. Hague, Investigation the Effect of Particle Size Distribution on Processing Parameters Optimisation in Selective Laser Melting Process, *Sff.* (2011) 227–238.
- [13] M. Averyanova, P. Bertrand, B. Verquin, Influence of metallurgical aspects of martensitic stainless steel powder on final parts properties manufactured by Selective Laser Melting technology, *Proc. PM2010 Powder Metall. World Congr. 10th – 14th Oct. 2010, Florence, Italy Publ. by Eur. Powder Metall. Assoc. 2010.* (2010) paper N° 514 – pp2–9.
- [14] M. Averyanova, P. Bertrand, B. Verquin, Studying the influence of initial powder characteristics on the properties of final parts manufactured by the selective laser melting technology, *Virtual Phys. Prototyp.* 6 (2011) 215–223. doi:10.1080/17452759.2011.594645.
- [15] S.F. Franzen, M. Svensson, I. Elfstrom, U. Ackelid, I. Elfstrom, Influence of powder size and layer thickness on the properties of Ti-6Al-4V lattice structures manufactured by electron beam melting, *Eur. Int. Powder Metall. Congr. Exhib. Euro PM 2011, Oct. 9, 2011 - Oct. 12, 2011.* 2 (2011) 825–834.
- [16] L.C. Ardila, F. Garcíandia, J.B. González-Díaz, P. Álvarez, a. Echeverria, M.M. Petite, R. Deffley, J. Ochoa, Effect of IN718 Recycled Powder Reuse on Properties of Parts

- Manufactured by Means of Selective Laser Melting, *Phys. Procedia*. 56 (2014) 99–107. doi:10.1016/j.phpro.2014.08.152.
- [17] V. Seyda, N. Kaufmann, C. Emmelmann, Investigation of Aging Processes of Ti-6Al-4 V Powder Material in Laser Melting, *Phys. Procedia*. 39 (2012) 425–431. doi:10.1016/j.phpro.2012.10.057.
- [18] S.A. Khairallah, A. Anderson, Mesoscopic simulation model of selective laser melting of stainless steel powder, *J. Mater. Process. Technol.* 214 (2014) 2627–2636. doi:10.1016/j.jmatprotec.2014.06.001.
- [19] D. Dai, D. Gu, Thermal behavior and densification mechanism during selective laser melting of copper matrix composites: Simulation and experiments, *Mater. Des.* 55 (2014) 482–491. doi:10.1016/j.matdes.2013.10.006.
- [20] a. V. Gusarov, I. Smurov, Modeling the interaction of laser radiation with powder bed at selective laser melting, *Phys. Procedia*. 5 (2010) 381–394. doi:10.1016/j.phpro.2010.08.065.
- [21] F. Verhaeghe, T. Craeghs, J. Heulens, L. Pandelaers, A pragmatic model for selective laser melting with evaporation, *Acta Mater.* 57 (2009) 6006–6012. doi:10.1016/j.actamat.2009.08.027.
- [22] M. Simonelli, C. Tuck, N.T. Aboulkhair, I. Maskery, I. Ashcroft, R.D. Wildman, R. Hague, A Study on the Laser Spatter and the Oxidation Reactions During Selective Laser Melting of 316L Stainless Steel, Al-Si10-Mg, and Ti-6Al-4V, *Metall. Mater. Trans. A.* (2015). doi:10.1007/s11661-015-2882-8.
- [23] M.J. Zhang, G.Y. Chen, Y. Zhou, S.C. Li, H. Deng, Observation of spatter formation mechanisms in high-power fiber laser welding of thick plate, *Appl. Surf. Sci.* 280 (2013) 868–875. doi:10.1016/j.apsusc.2013.05.081.
- [24] Y. Liu, Y. Yang, S. Mai, D. Wang, C. Song, Investigation into spatter behavior during selective laser melting of AISI 316L stainless steel powder, *Mater. Des.* 87 (2015) 797–806. doi:10.1016/j.matdes.2015.08.086.
- [25] A. Ladewig, G. Schlick, M. Fisser, V. Schulze, U. Glatzel, Influence of the shielding gas flow on the removal of process by-products in the selective laser melting process, *Addit. Manuf.* 10 (2016) 1–9. doi:10.1016/j.addma.2016.01.004.
- [26] B. Ferrar, L. Mullen, E. Jones, R. Stamp, C.J. Sutcliffe, Gas flow effects on selective laser melting (SLM) manufacturing performance, *J. Mater. Process. Technol.* 212 (2012) 355–364. doi:10.1016/j.jmatprotec.2011.09.020.
- [27] P.Y. Shcheglov, a V Gumenyuk, I.B. Gornushkin, M. Rethmeier, V.N. Petrovskiy, Vapor–plasma plume investigation during high-power fiber laser welding, *Laser Phys.* 23 (2013) 016001. doi:10.1088/1054-660X/23/1/016001.
- [28] G.R. Mirshekari, E. Tavakoli, M. Atapour, B. Sadeghian, Microstructure and corrosion

behavior of multipass gas tungsten arc welded 304L stainless steel, Mater. Des. 55 (2014) 905–911. doi:10.1016/j.matdes.2013.10.064.